Characterization of a Friction-Stir-Welded Aluminum Alloy 6013

BEATE HEINZ and BIRGIT SKROTZKI

The aluminum alloy 6013 was friction-stir welded in the T4 and the T6 temper, and the microstructure and mechanical properties were studied after welding and after applying a postweld heat treatment (PWHT) to the T4 condition. Optical microscopy (OM), transmission electron microscopy (TEM), and texture measurements revealed that the elongated pancake microstructure of the base material (BM) was transformed into a dynamically recrystallized microstructure of considerably smaller grain size in the weld nugget. Strengthening precipitates, present before welding in the T6 state, were dissolved during welding in the nugget, while an overaged state with much larger precipitate size was established in the heat-affected zone (HAZ). Microhardness measurements and tensile tests showed that the HAZ is the weakest region of the weld. The welded sheet exhibited reduced strength and ductility as compared to the BM. A PWHT restored some of the strength to the as-welded condition.

I. INTRODUCTION

MODERN aerospace concepts demand reductions in both the weight as well as the cost of the production of materials. Therefore, welding processes have proven most attractive, and programs have been set up to study their potential.[1] Car manufacturers and shipyards are also evaluating new production methods.[2,3] Laser-beam welding and friction-stir welding (FSW) are currently considered to be the most prospective welding processes. Friction stir welding is a novel friction-welding process recently developed by TWI (The Welding Institute, Cambridge, U.K.) for nonferrous materials.[4] It is a solid-state process generating frictional heat between a rotating tool and the material being welded. A softened plasticized region is created around the tool, and consequently, the plasticized material is extruded from the leading side to the trailing side of the tool as it is steadily moved along the joint line.[5] Neither filler material nor shielding gas is required. As the melting temperature is not reached, there is no volume change during joining, and it is generally agreed that FSW gives rise to low residual stresses after welding. However, experimental measurements have shown that longitudinal residual stresses cannot be neglected.[6] The heat developed by a combination of friction and plastic work is relatively small when compared to fusion welding, and therefore, warp and shrinkage are low. Alloys that are not considered as being weldable (due to pores or crack formation) and even metal-matrix composites can be joined by FSW. Potential applications of FSW in the aerospace industry are in the field of joining fuselage, structural parts, and cryogenic tanks.[5] Joining of panels and large extruded profiles is also an interesting application for FSW, and it is used now in series in ship, bridge, and wagon building and in offshore industry.[2,3,7]

The FSW technology is developing rapidly. It can be applied to all Al alloys and even dissimilar Al alloys can be joined. However, the microstructural changes that occur during the FSW process combined with the mechanical properties after welding are only now being reported.[6,8–16] Modeling is presently used to explain the physical and mechanical details of the FSW process.[17,18]

The material with a high potential to replace the currently used AlCuMg-alloy 2024 for welded parts is the AlMgSiCu-alloy 6013. This alloy, when compared to the 2024 Al alloy, shows about 10 pct less strength at the same density, comparable corrosion resistance, and the same production cost. Generally, 6xxx series alloys are widely used because of their good weldability, corrosion resistance, and immunity to stress-corrosion cracking and are, therefore, used for the majority of extrusions.[19] The alloy 6013 is a recent development, and its envisaged application is seen in the aircraft, automotive, and recreation industries.[19]

Precipitation processes in the Al-Mg-Si system have been studied for many years. However, results are not unequivocal. As in many other age hardenable Al-alloy systems, a precipitation sequence of metastable phases is observed in this alloy before the stable phase, β-Mg_2Si, is formed. Most recent studies propose the following sequence: independent cluster of Mg and Si $\rightarrow$ cocluster of Mg and Si $\rightarrow$ needle-shaped β'' $\rightarrow$ rod-shaped β' $\rightarrow$ plate-shaped β-Mg_2Si.[20,21] Guinier-Preston zones consist of fine plates of monolayer thickness, 2.5-nm width and $<$20-nm length.[22] Its elongated direction is parallel to $\langle 100 \rangle_{Al}$. A number of crystal structures have been proposed for the intermediate phases β'' and β'. Anderson *et al.*[24] reported that β'' is C-centered monoclinic with lattice parameters, $a = 1.516$ nm, $b = 0.405$ nm, $c = 0.674$ nm, and $\beta = 105.3$ deg. The orientation relationship was found to be $(001)_{Al} \parallel (010)_{\beta''}$ and $[310]_{Al} \parallel [001]_{\beta'}$.[21] Edwards *et al.*[21] obtained very similar results. The composition of β'' is reported to be close to Mg:Si = 1:1[21,23,25] or 5:6[24] in alloys with Si excess. For β', a hexagonal-crystal structure with $a = 0.71$ nm and $c = 0.405$ nm was recently proposed.[26] The orientation relationship is $(100)_{Al} \parallel (0001)_{\beta'}$ and $[110]_{Al} \parallel [\bar{1}100]_{\beta'}$. Some authors report on the occurrence of an additional precipitate named B', which is lath-shaped and has a hexagonal structure with $a = 1.04$ nm and $c = 0.405$ nm.[21,26,27]

BEATE HEINZ, R&D Engineer, formerly with the Department of Mechanical Engineering, Institute for Materials, Ruhr-University Bochum, is with Faurecia Autositze GmbH & Co. KG, Stadthagen, Germany. BIRGIT SKROTZKI, Chief Engineer, is with the Department of Mechanical Engineering, Institute for Materials, Ruhr-University Bochum, 44780 Bochum, Germany. Contact e-mail: birgit.skrotzki@ruhr-uni-bochum.de

Manuscript submitted February 27, 2001.

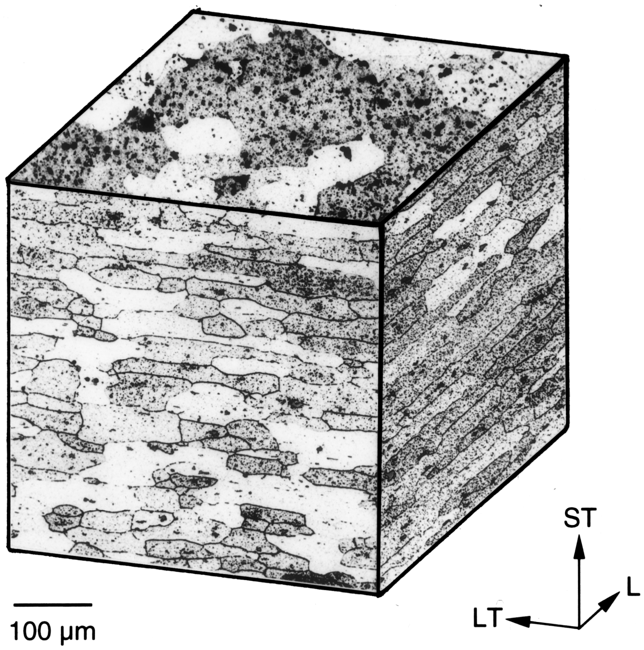

Fig. 1—Optical micrograph of the rolled BM 6013.

In Cu-containing Al-Mg-Si alloys, a quaternary stable phase, Q, is formed.[25,26,27] Its exact composition is not yet known. The crystal structure of the Q phase is hexagonal with lattice parameters $a = 1.04$ nm and $c = 0.405$ nm.[26] Its metastable precursor is called Q' (sometimes also named L or λ') with the same crystal structure as the equilibrium phase, but unlike Q, it is coherent to the matrix.[27] The Q' metastable precursor has a lath morphology with its long axis parallel to $\langle 001 \rangle_{Al}$ and with {150} habit plane. The orientation relationship is given to be $(010)_{Al} \parallel (21\bar{3}0)_{Q'}$ and $[001]_{Al} \parallel [0001]_{Q'}$.[27]

The alloy 6013 was investigated to allow comparison of FSW welds with laser-beam welded joints. The objective of the present work was to characterize the microstructure of the nugget and of the heat-affected zone (HAZ) as compared to the base material (BM) of alloy 6013. Microscopic and X-ray diffraction techniques were combined with microhardness measurement and tensile tests to understand the interaction between the welding tool and the resulting flow of the material and the microstructural changes associated with the welding process.

II. EXPERIMENTAL

A 4-mm-thick rolled sheet of alloy 6013 (Figure 1) was friction stir welded in the T4 (solution heat treated at 565 °C to 570 °C and water quenched followed by natural aging at room temperature for at least 21 days) and T6 (solution heat treated and quenched (as in T4), artificial aging at 190 °C/4 hours, followed by air cooling) conditions. For solution heat treatment and artificial aging, the sheets were placed in the hot furnace, and therefore, the time to heat the samples to solution and age temperature was short. A postweld heat treatment (PWHT), which consisted of heating in an air furnace at 190 °C for 4 hours, was applied to the welded T4 sheet (T4 + PWT) to improve strength due to precipitation hardening. The chemical composition of the BM is given in Table I. The FSW tool rotated with 1400 rpm, and the linear welding speed was 400 mm/min (T6) and 450 mm/min (T4), respectively. The material was either investigated in the as-FSW condition (T4, T6) or in the postweld heat-treated condition (T4 + PWT).

Table I. Chemical Composition of the 6013 BM

Element	Mg	Si	Cu	Mn	Fe	Cr	Zn	Ti	Al
Wt pct	0.90	0.72	0.95	0.36	0.27	0.03	0.07	0.02	bal

Standard metallographic techniques were applied to prepare samples for optical microscopy (OM) and transmission electron microscopy (TEM). The TEM samples were electrolytically polished (using the twin-jet method) in a solution of 30 vol pct nitric acid and 70 vol pct methanol at −30 °C and $U = 15$ V. A PHILIPS* CM20/STEM microscope was used for conventional TEM to characterize the microstructure by bright field (BF), dark field (DF), and selected area diffraction (SAD) techniques. The TEM foils were prepared from the BM, the HAZ, and the nugget to study the microstructure in these regions.

*PHILIPS is a trademark of Philips Electronic Instruments Corp., Mahwah, NH.

Vickers microhardness measurements (HV 0.05, *i.e.*, 0.49-N load) were carried out across the weld, *i.e.*, normal to the welding direction, at sheet thickness, t, of t/8 (close to the top), t/2 (center), and 7t/8 (close to the bottom), to study the variation in hardness with distance from the centerline of the weld.

Tensile properties were evaluated transverse to the weld. The gauge length of the tensile specimens was 50 mm. The thickness was 2.5 mm, *i.e.*, the surface was machined off. Duplicate tests were conducted for each condition. The local strain was measured in the weld and in the BM. A grid with an initial mesh size of 200 μm (± 3 μm) was applied to the surface of the undeformed tensile samples by using a photographic technique. The mesh size of the deformed state was measured using a measuring microscope.

Microhardness measurements and tensile tests were carried out about 4 months after welding.

The X-ray diffraction studies were conducted using a PHILIPS X'pert MRD system with a copper target ($\lambda = 0.15405$ nm) at $U = 40$ kV and $I = 40$ mA. The texture of the Al sheet and of the weld was determined by measuring the (111), (200), and (220) pole figures at the top surface ($t = 0$) and at half-sheet thickness, t/2. Oscillation of 5 mm was applied during the measurement of the BM to increase the volume penetrated by the X-ray beam. The FSW samples did not oscillate because the analysis had to focus on the welded area. All samples were electropolished to remove the deformation layer on the surface formed by grinding and polishing. An X-ray lens (parallel-beam optic) was used with a beam dimension of 2 × 2 mm, which provides higher intensities as compared to the fixed divergence slit. Experimental pole-figure data were corrected for background and defocusing. Subsequently, the orientation distribution function (ODF) was calculated using the PHILIPS X'pert Texture Software package.

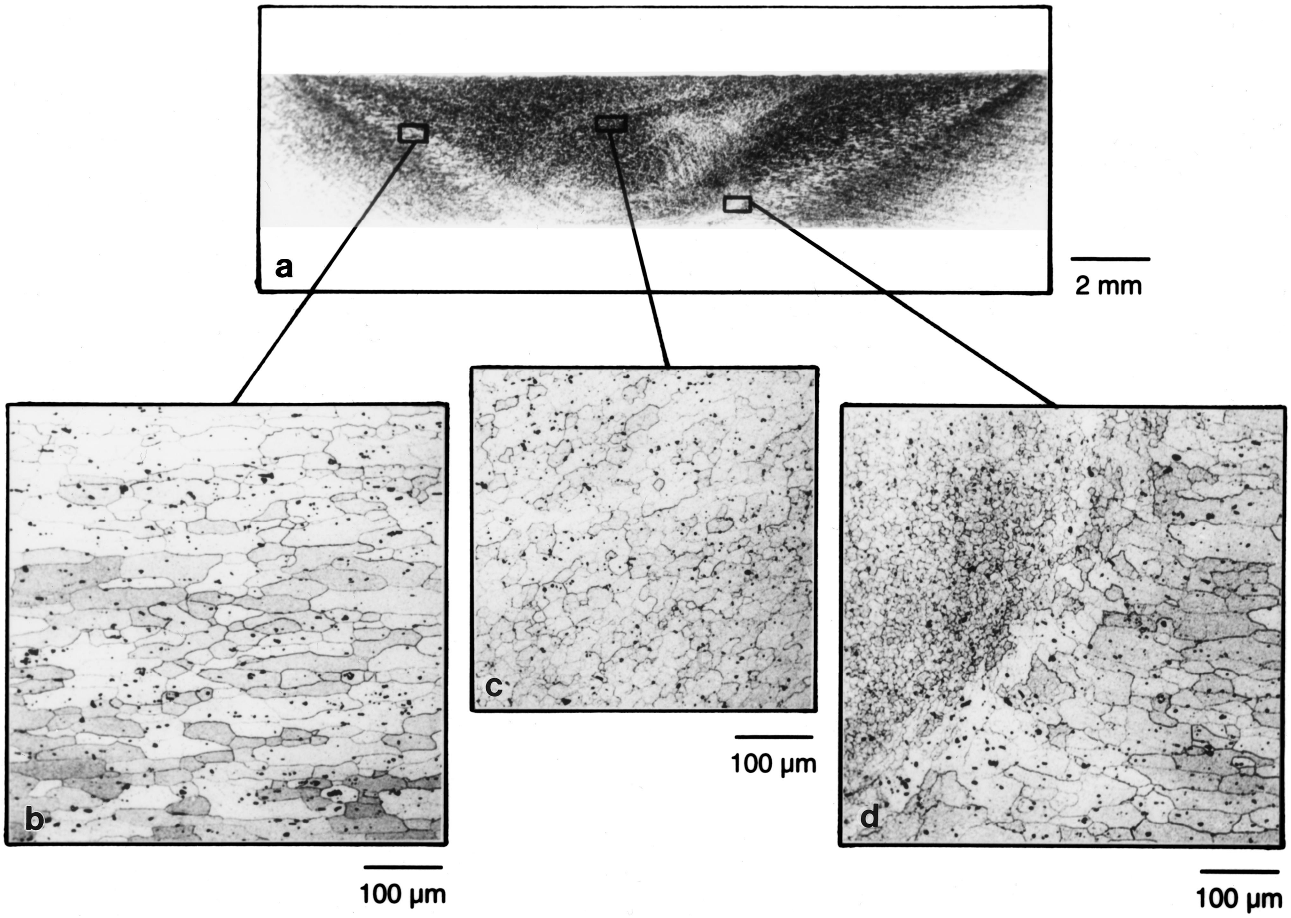

Fig. 2—6013 T6: (*a*) Overview of the cross section perpendicular to the welding direction; and (*b*) through (*d*) details of the microstructure at higher magnification (OM).

III. MICROSTRUCTURE

An optical micrograph of the welded sheet material is shown in Figure 2. The weld zone is clearly visible in the low-magnification overview of Figure 2(a) because of its different contrasts developed after etching. The welding direction is in the line of sight. The weld zone is V-shaped and widens near the top surface because of the close contact between the shoulder of the tool and the upper surface. A weld nugget was barely noticeable and not very distinct. (Nevertheless, the term "nugget" is used in the following to distinguish this zone from the entire weld region.) The shape of the weld zone likely depends on the welding parameters and the material.[20]

While the rolled BM is characterized by elongated pancake-shaped grains in the L/ST and LT/ST planes (Figure 1), the nugget shows rather equiaxed grains. The mean grain size of the BM in the LT/ST plane was measured to be $d_{max} = 62$ μm and $d_{min} = 20$ μm with an aspect ratio of 3.1. The HAZ shows a comparable grain size of $d_{max} = 59$ μm and $d_{min} = 17$ μm (Figure 2(b)). The mean grain size of the weld nugget was found to vary between 10 and 15 μm (Figure 2(c)). However, even smaller grains of about 8-μm size were found close to the bottom of the welded sheet (Figure 2(d)). The considerably smaller grain size of the nugget combined with the equiaxed shape implies that dynamic recrystallization (DRX) has taken place during FSW because of deformation and temperature, which may reach 0.8 T_m.[8,10,20,28–31] This is in agreement with observations made by other authors.[6,8–11,13–15,20] The small equiaxed grains of the weld nugget were also found in the TEM foils

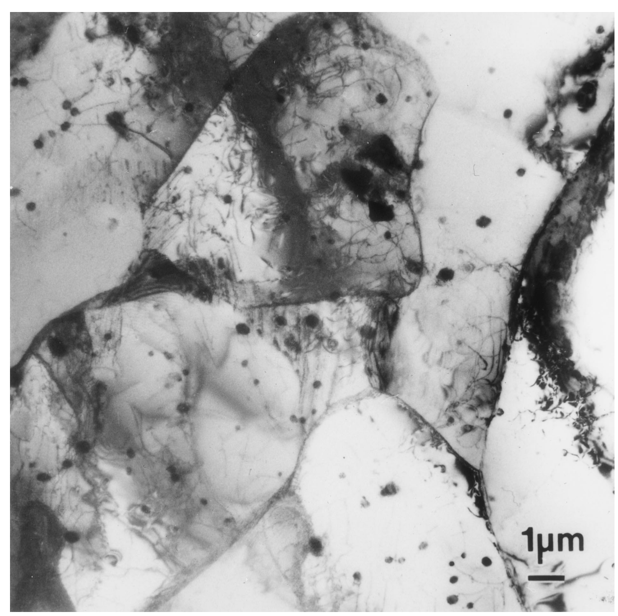

Fig. 3—TEM micrograph of the weld nugget. Small equiaxed grains show subgrains in their interior.

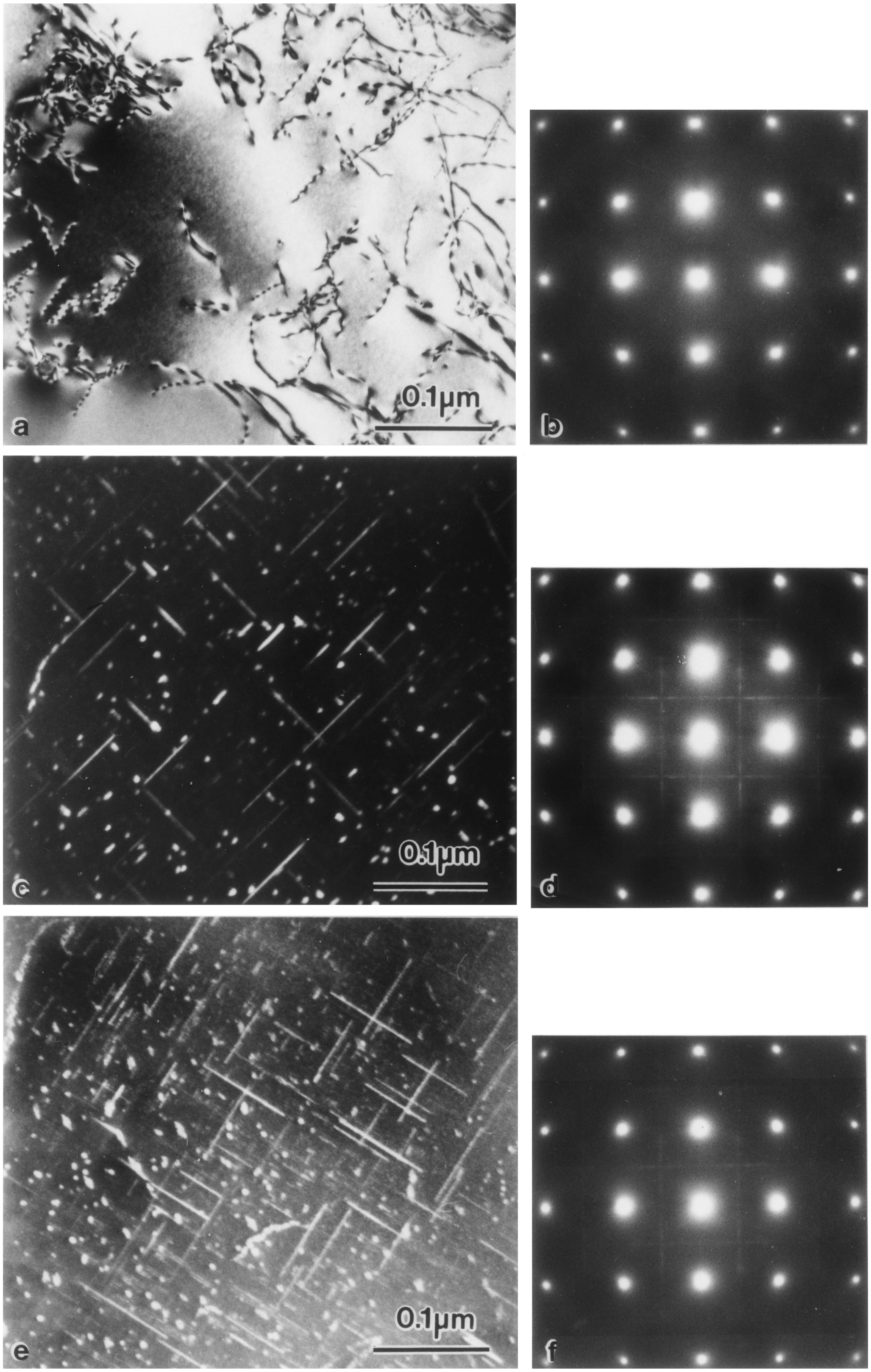

Fig. 4—TEM micrographs of the BM in the (*a*) and (*b*) T4, (*c*) and (*d*) T6, and (*e*) and (*f*) T4 + PWT condition.

(Figure 3). The interiors of such grains are composed of subgrains implying that deformation has continued after DRX has occurred. Subgrains were also found in the HAZ, although the grain size was larger and the grains were elongated. The grain boundaries of the HAZ were densely populated with precipitates, which contain Al, Mg, Si, and Cu.

Figure 4 shows TEM micrographs of the BM. In the T4 condition, no evidence of precipitates was found in BF

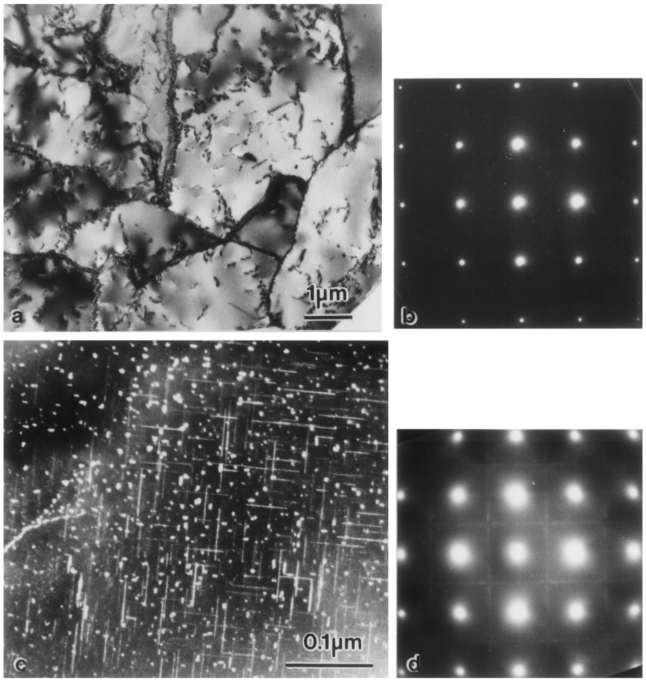

Fig. 5—TEM micrographs of the weld nugget in the (*a*) and (*b*) T6 and (*c*) and (*d*) T4 + PWT condition.

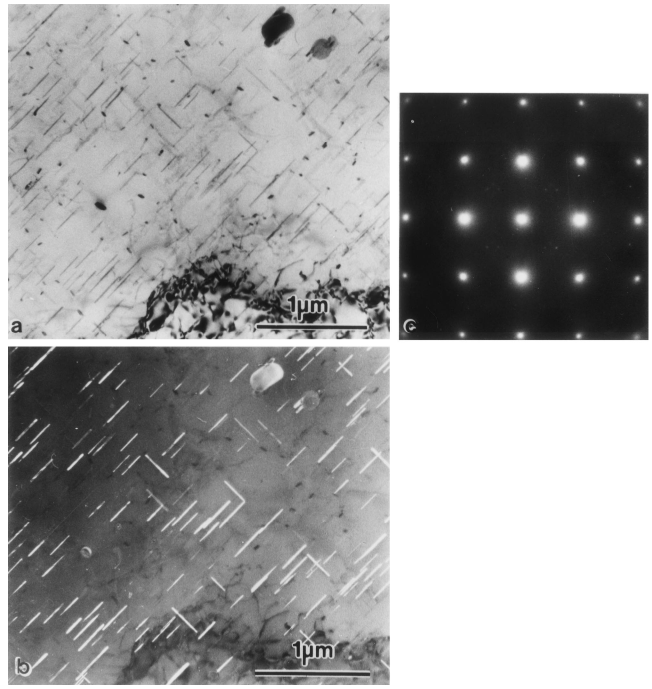

Fig. 6—TEM micrographs of the HAZ of the T6 sheet: (*a*) BF and (*b*) DF image taken close to $\langle 001 \rangle_{Al}$ (*c*) $[001]_{Al}$ SAD pattern.

images or in standard SAD patterns. The BF image in Figure 4(a) shows a few dislocations. The $\langle 001 \rangle_{Al}$ SAD pattern of Figure 4(b) provides no indication for any additional phases beside aluminum. Figure 4(c) shows a DF image (taken close to $\langle 001 \rangle_{Al}$ zone axis) of the T6 condition, and now an array of needle-shaped precipitates of about 50-nm length is observed. The SAD pattern in Figure 4(d) is characterized by streaks along the $[100]_{Al}$ and $[010]_{Al}$ directions, which indicate the presence of precipitates along these directions. The BM in the T4 + PWT conditions exhibits a very similar structure to the T6 condition. Figures 4(e) and (f) again show needle-shaped precipitates in the DF image and streaks in the $\langle 001 \rangle_{Al}$ SAD pattern.

The TEM micrographs of the weld nugget are shown in Figure 5. Figures 5(a) and (b) were taken on the T6 sheet. Figure 5(a) shows that the small recrystallized grains of the weld nugget contain subgrains. The SAD patterns of these regions did not reveal any streaks. This indicates that the precipitates present in the T6 condition dissolve during FSW, which is well in agreement with Sato *et al.*[20] and Liu *et al.*,[29] who welded 6063 and 6061 sheet materials, respectively. Jata *et al.*[6] also observed dissolution of hardening precipitates in a friction-stir-welded 7050 alloy. In the T4 sheet (not shown), the weld nugget was also free of precipitates. However, after receiving a PWHT, precipitates were found, as is shown in Figures 5(c) and (d). The DF image (taken close to $\langle 001 \rangle_{Al}$) of Figure 5(c) again shows needle-shaped precipitates of about 50-nm length, and streaks are present in the $\langle 001 \rangle_{Al}$ diffraction pattern.

The HAZ is characterized (for all three conditions studied in the present work) by elongated grains (*cf.* Figure 2(b)) and by grain boundaries decorated by particles. The TEM micrographs of the HAZ show much larger precipitates in the grain interior when compared to the BM. Figure 6 shows (as an example for all conditions) images taken from the T6 sheet. The precipitates are already visible in the BF image (Figure 6(a)). Figure 6(b) is a DF image and shows rather lath-shaped precipitates of about 280-nm length. Both figures were taken close to the $\langle 001 \rangle_{Al}$ zone axis. No streaks were present in the SAD pattern of Figure 6(c). However, beside Al-matrix spots, there are additional spots, which are caused by the precipitates. This microstructure represents an overaged condition due to the temperature brought in by the FSW process. Again, this agrees well with the observations reported in the literature.[6,20,28]

IV. TEXTURE MEASUREMENTS

The texture measurements show that the texture in the BM is not the same at $t/2$ and at the sheet surface. The (111) pole figures of the 6013-T6 samples studied are given in Figure 7. Figures 7(a) and (c) represent the pole figures of the sheet in the center and at the top surface, respectively. It is well known that the rolling texture varies with sheet thickness because of the larger shear component at the surface during rolling deformation.[33] The pole figures in Figure 7 also reveal that the texture in the weld region is quite different from that in the BM. Figures 7(b) and (d) show (111) pole figures of the weld at $t/2$ and $t = 0$, respectively.

More detailed information on the texture can be obtained from the ODFs calculated from the three experimentally measured, pole figures. Texture components and their intensities can be identified, and the results of this analysis are summarized in Figure 8 for the major texture components found in our material. Figure 8 shows the density, $f(g)$ (in times random), of seven texture components with their Miller indices given in Table III.[34] At $t/2$, the strongest component of the BM is A (28 times random), followed by the Copper and Goss component, while at the surface, very high densities are found for the S (64 times random) and Cube (41 times random) components. In contrast, the weld exhibits

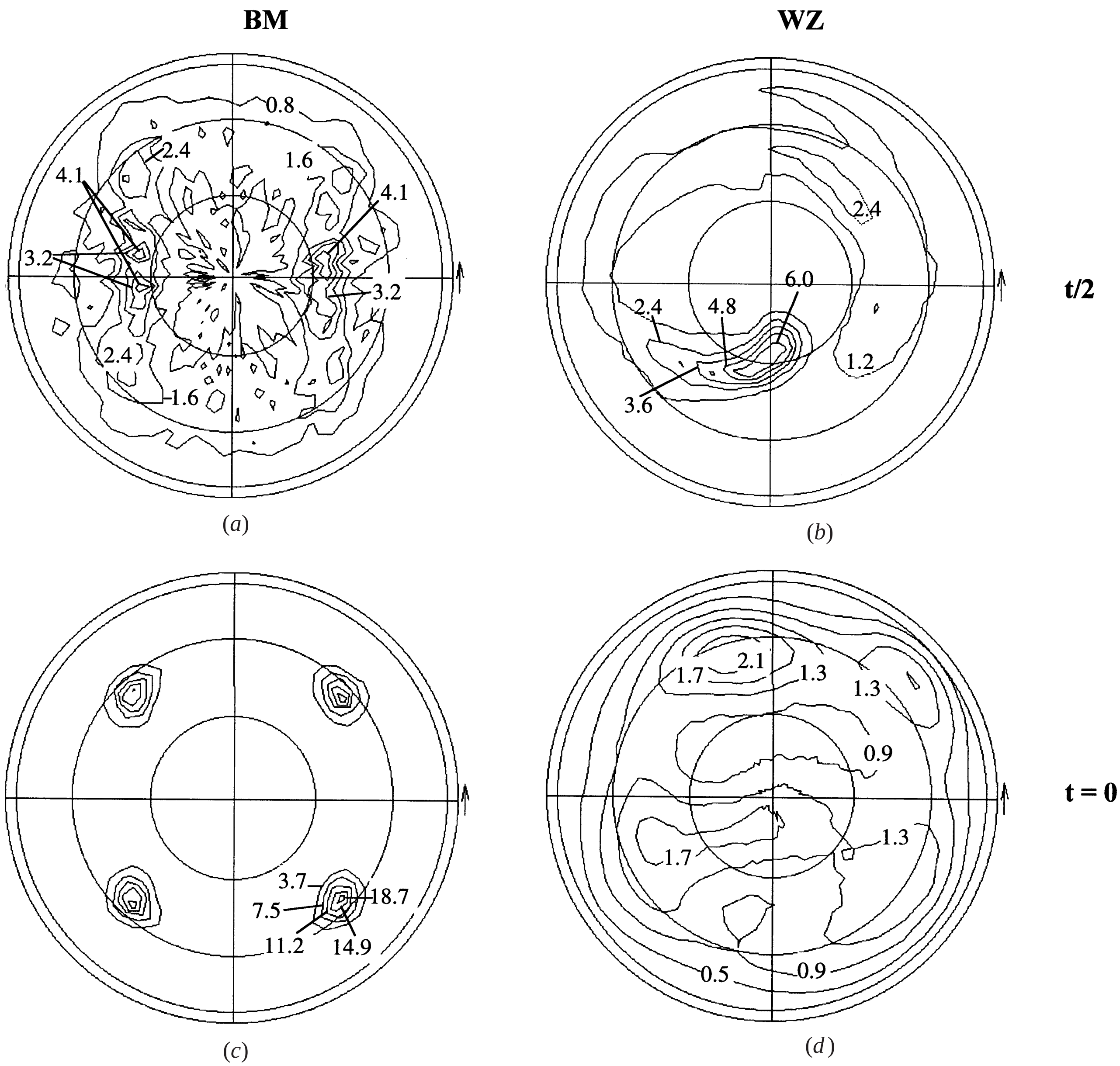

Fig. 7—(111) pole figures of 6013-T6 sheet. (*a*) Base material and (*b*) weld region at *t*/2. (*c*) Base material and (*d*) weld at top surface ($t = 0$).

much weaker and also different texture components. At half-sheet thickness, the major component is A (9 times random) followed by W_{RD}, while at $t = 0$ the only noticeable component is W_{RD} (2 times random). Copper and S (and B) are typical rolling-texture components in Al alloys, while Cube, Goss, and W_{RD} represent recrystallization components.[33,35]

V. DYNAMIC RECRYSTALLIZATION

Aluminum and its alloys normally do not undergo discontinuous dynamic recrystallization (DDRX) because of their high level of recovery due to aluminum's high stacking-fault energy.[33,37] However, particle-stimulated nucleation of DRX is observed in alloys with large ($>$0.6 μm) secondary particles.[33–38] The DDRX is characterized by nucleation and growth of new grains at old high-angle grain boundaries[39] (although the nucleation mechanism has not yet been positively identified[33]). Beside DDRX (or conventional DRX) other mechanism of DRX are described in the literature, which produce high-angle grain boundaries during high-temperature deformation. Formation processes different from nucleation and growth of grains characterize these types of DRX. Two alternative mechanisms were proposed for Al alloys, *i.e.*, continuous DRX (CDRX) and geometric DRX (GDRX).[33,37,39] The CDRX (or rotation recrystallization) is characterized by a strain-induced progressive rotation of subgrains with little boundary migration. The rotated subgrains are gradually transformed into grain boundaries. It occurs in high-alloyed Al-Mg and Al-Zn alloys.[39] The GDRX is common in Al alloys after high strains. During large deformation by hot rolling or hot compression, grains flatten and grain boundaries become serrated because of dynamic recovery. Finally, the flattened grain boundaries come into contact and annihilate, which results in a microstructure of small equiaxed grains.[33,39] It appears that the mechanism operating during FSW and resulting in a dynami-

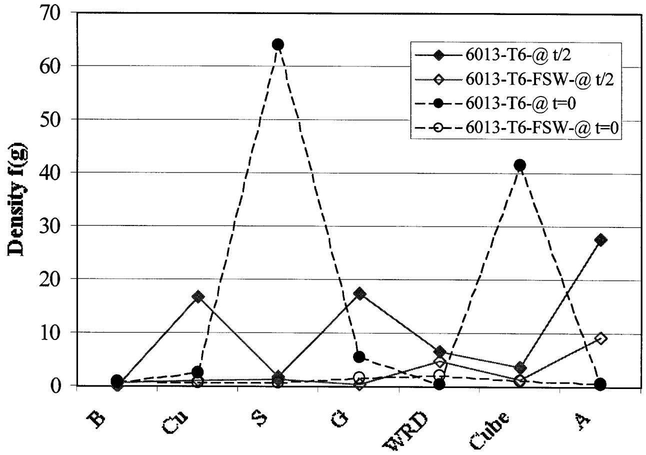

Fig. 8—Density (in times random) of major texture components in the base material (full symbols) and in the weld (open symbols) at $t/2$ and at the top surface.

cally recrystallized microstructure is in agreement with the subgrain rotation model assisted by dislocation glide.

VI. MICROHARDNESS MEASUREMENTS

The microhardness was measured at half-sheet thickness ($t/2$) and close to the bottom ($7t/8$) and the top ($t/8$) of the welded sheet. The results are shown for the T4 (Figure 9(a)) and T6 (Figure 9(c)) conditions. The weld zone is considerably softer than the BM. This softening is observed within about 13 to 15 mm of both sides of the weld centerline ($x = 0$). The three hardness profiles differ (for all heat-treatment conditions) in the sense that close to the top of the sheet ($t/8$), the minimum hardness values of 95 to 100 HV were measured about 10 mm away from the center while that close to the bottom ($7t/8$) were found to be about 6 mm away from the center (Figure 9). The minimum hardness measured at half-sheet thickness was found to be in between. Close to the top, the minimum hardness values are associated with a sharp dip of the hardness curve. This minimum dip widens from the top to the bottom, and consequently, the plateau region (with a higher hardness than the minimum value) observed around the centerline of the weld narrows. The microhardness curves correspond well with the geometry of the V-shaped weld shown in Figure 2(a).

In the T4 condition, the microhardness decreases from 120 HV in the BM to around 100 HV in the center of the weld (Figure 9(a)). A PWHT of 4 hours at 190 °C increases the hardness both in the center of the weld and in the BM to about 140 HV, while the minima are still present (Figure 9(b)). The sheet welded in the T6 condition (Figure 9(c)) showed a base-metal hardness of about 140 HV, while lower values of about 110 HV were observed around the centerline of the weld.

Similar results with respect to the shape of the microhardness curves were reported by Jata *et al.*[6] and Sato *et al.*[20] The HAZ is soft, and Mahoney *et al.*[8] have shown that it behaves in a ductile manner during mechanical loading. The effect of a PWHT seems to depend strongly on the alloy system and the heat treatment before welding. Jata *et al.*[6] reported that the hardness of the weld increased while that of the BM is only little affected by the PWHT. Mahoney *et al.*[8] did not observe any increase in the strength after PWHT of their alloy. However, these 7xxx alloys were in the T7 condition before welding. In contrast, the material in the present study chosen for PWHT was in the T4 condition, which has a high potential left for precipitation during a heat treatment following the welding process.

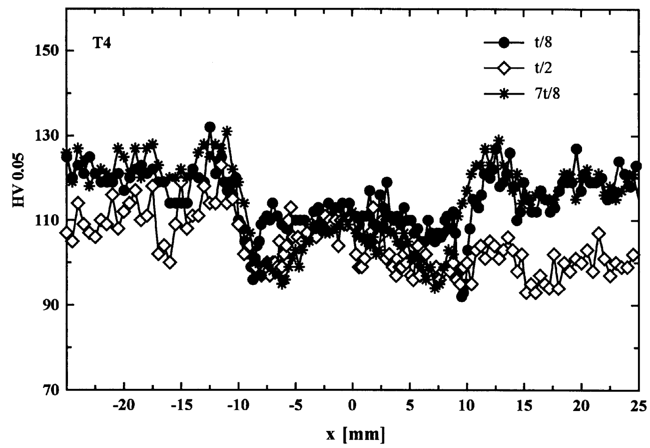

(*a*)

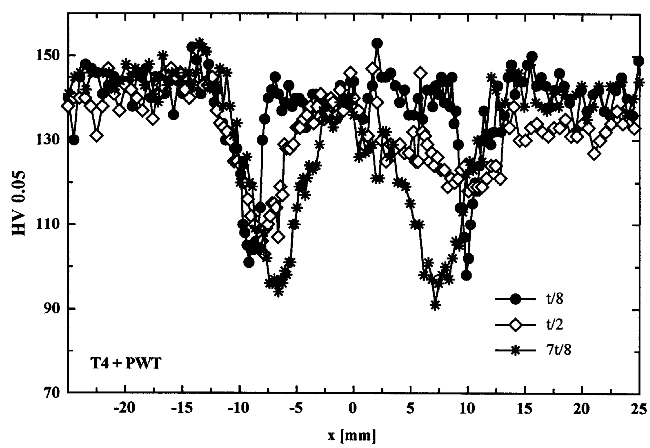

(*b*)

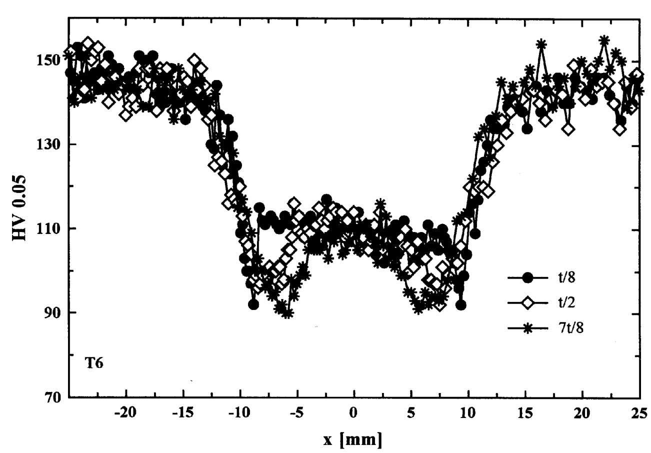

(*c*)

Fig. 9—Microhardness profiles for the top ($t/8$), center ($t/2$), and bottom ($7t/8$) of the FSW sheet in the (*a*) T4, (*b*) postweld heat-treated T4, and (*c*) T6 condition. Centerline of weld is at $x = 0$.

Table II. Tensile Properties of Alloy 6013 before[32] and after Welding

Condition	Postweld Treatment	σ_y (MPa)	UTS (MPa)	ε_f (Pct)	Joint Efficiency
T4 (BM)	—	222	320	20.5	—
T6 (BM)	—	357	394	11.5	—
T4 + FSW	—	160	300	8.7	0.94
T4 + FSW	4h/190 °C	247	323	1.2	0.82
T6 + FSW	—	165	295	4.5	0.75

Table III. Miller Indices of Texture Components Used in Figure 8[34]

Notation	Miller Indices $\{hkl\}\langle uvw\rangle$
Brass (B)	$\{011\}\langle 21\bar{1}\rangle$
Copper (Cu)	$\{112\}\langle 11\bar{1}\rangle$
S	$\{123\}\langle 63\bar{4}\rangle$
Goss (G)	$\{011\}\langle 100\rangle$
W_{RD}	$\{025\}\langle 100\rangle$
Cube	$\{001\}\langle 1\bar{0}\bar{0}\rangle$
A	$\{112\}\langle \bar{1}10\rangle$

VII. TENSILE TESTS

Tensile tests in the T4, the T4 PWHT, and the T6 condition showed that fracture always occurred in the HAZ. Failure took place as a 45 deg shear fracture and was accompanied with some necking. This was also observed by Mahoney *et al.*[8] Failure always occurred on the advancing side of the weld. The tensile properties of our material are given in Table II. Compared to the BM, specimens tested transverse to the weld exhibit reduced strength and ductility. The PWHT restored some of the strength to the as-welded condition. However, the elongation at fracture was considerably reduced from 8.7 to 1.2 pct.

The joint efficiency (ultimate tensile strength, UTS_{weld}/UTS_{BM}) is highest in the sheet, which was welded in the T4 condition (94 pct) and lowest in the one welded in the T6 state (75 pct) (*cf.* Table II).

VIII. LOCAL STRAIN MEASUREMENTS

The data of the local strain measurements are represented in Figure 10 together with the microhardness curves determined at *t*/8. It becomes clear from Figure 10 that for all conditions, the maximum local strain is always concentrated in the HAZ, which is the softest region (as the microhardness measurements have revealed) and strain values of up to 40 pct were observed. For the T4 sheet (Figure 10(a)), strains of 5 to 10 pct were measured in the weld nugget and in the BM because of the low resistance to deformation after the T4 heat treatment, resulting in a high macroscopic-fracture strain of 8.7 pct (Table II). The T6 sheet shows some local strain (5 to 10 pct) in the weld nugget, while there is negligible deformation in the BM (Figure 10(c)). This can be explained by the softness of the weld nugget caused by dissolution of the hardening precipitates and by the high strength of the BM after the T6 treatment. After postweld heat treating the T4 sheet, the strain is very localized in the HAZ (Figure 10(b)), which also explains the low macroscopic-fracture strain of 1.2 pct of this condition (*cf.* Table

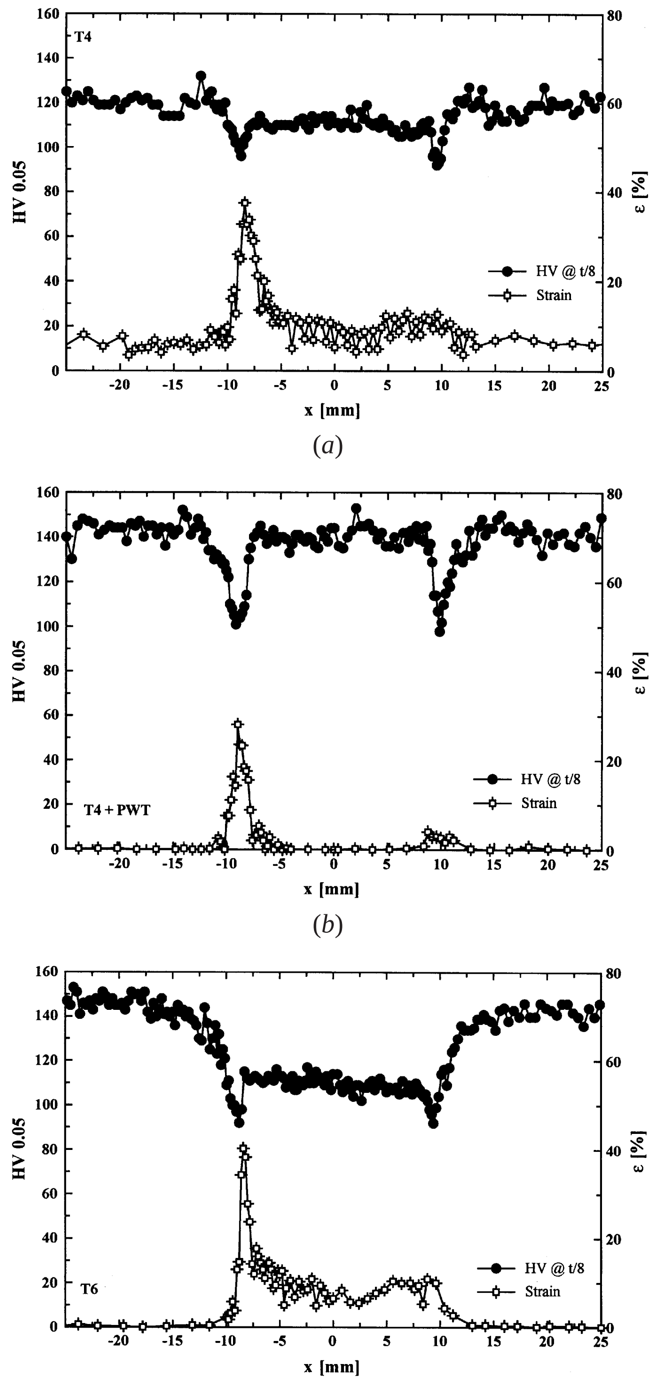

Fig. 10—Local strain (right axis) and microhardness at *t*/8 (left axis) of the FSW sheet in the (*a*) T4, (*b*) postweld heat-treated T4, and (*c*) T6 condition.

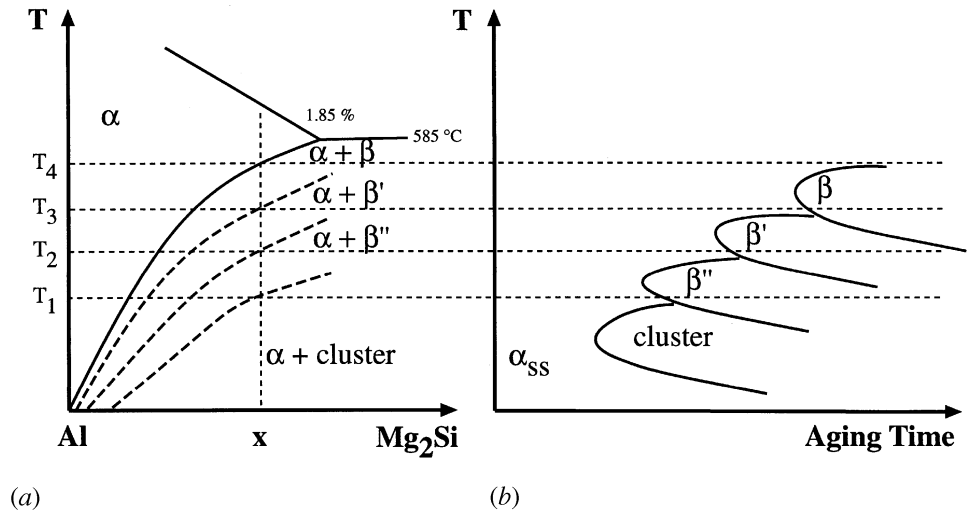

Fig. 11—(*a*) Phase diagram Al-β-Mg_2Si with metastable solvus lines and (*b*) continuous TTT diagram for the formation of clusters, β'', β' and equilibrium phase β.

II). The loss in ductility is a result of the age hardening of the BM and the nugget, which results in a high resistance to deformation, and of the overaged precipitation state in the HAZ, which causes localization of deformation in the latter.

Similar results were obtained by Mahoney *et al.*,[8] although the local strains were lower in the 7xxx alloy that was used in their study.

IX. CONCLUSIONS

Friction stir welding of 6013 sheet material results in a dynamically recrystallized microstructure of the weld nugget in both the T4 and the T6 sheet. Temperature and strain are high enough during FSW to initiate DRX because of the frictional heat and the large deformation introduced by the welding process. In addition, strengthening precipitates present in the T6 sheet before welding were dissolved during FSW and, therefore, no precipitates were observed in the weld nugget after welding. On the other hand, the HAZ is characterized by an overaged precipitate structure. The schematic phase diagram Al-β-Mg_2Si and the time-temperature-transformation (TTT) diagram shown in Figure 11 allow discussion of the temperature distribution in the sheet during welding (Figure 12). Figure 11(a) represents a schematic quasibinary cut α-Al solid-solution β-Mg_2Si with the metastable solvus lines for clusters, β'', and β'. For a composition, *x*, the temperature range for the formation of *e.g.*, β'' precipitates (*i.e.*, $T_1 < T < T_2$) can be found. Applying higher temperatures than T_2 (or using longer aging times, as seen in Figure 11(b)) results in the formation of the β' or the equilibrium β phase. Combining the microstructural results with the information obtained from Figure 11, it can be concluded that the temperature distribution during FSW must have been as shown in Figure 12. The weld nugget has seen the highest temperature, which has presumably exceeded T_4 because the precipitates were dissolved during FSW. (Another possibility is that β'' has dissolved directly.) This results in a softening because of the absence of precipitate hardening by β''. The temperature probably increases somewhat toward the centerline of the weld, as has been shown by experimental measurements and finite element

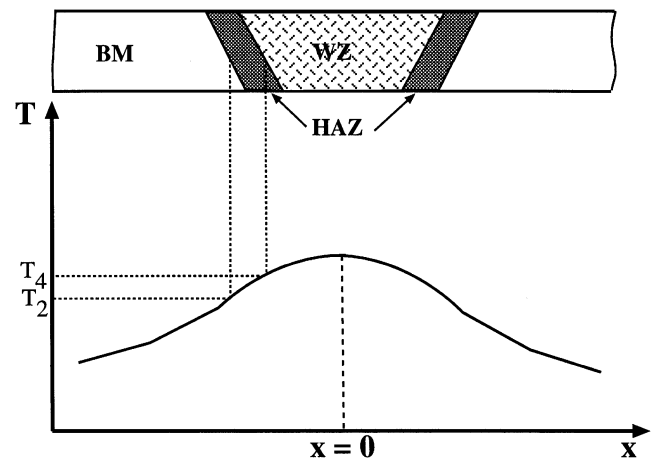

Fig. 12—Temperature distribution in the weld, the HAZ, and in the BM.

modeling of the temperature distribution.[18] The HAZ was heated up to temperatures of $T_2 < T < T_3$, and β' precipitates were found in those areas. Temperature is presumably more important than time because welding can be regarded as a rapid thermal cycle (although lower than compared to arc and laser welding) and heat flux into the Al BM is high. (Chao and Qi show calculated and measured data for the temperature history during FSW.[18]) The HAZ is in an overaged condition and, therefore, represents the weakest part of the welded material. The lowest hardness is found here, and failure in tensile tests always takes place in this area.

X. SUMMARY

The microstructure and mechanical properties of a friction stir welded Al-Mg-Si alloy (6013) was examined by OM, TEM, texture analysis, microhardness measurements, and tensile tests. The following results were obtained.

1 Friction stir welding results in a dynamically recrystallized grain structure in the weld nugget with smaller grain size than in the BM. Such dynamically recrystallized

grains are equiaxed compared to the elongated grains observed in the rolled BM.
2 The HAZ has a grain size similar to that of the BM.
3 Strengthening precipitates present prior to FSW are dissolved in the nugget. In the HAZ, precipitates coarsen and an overaged condition is established.
4 Microhardness measurements show that the nugget is softer than the BM, while minimum hardness values are found in the HAZ.
5 A PWHT of the T4 sheet increases the hardness in the BM as well as in the nugget but not in the HAZ. This heat treatment also increases the tensile strength of the weld.

ACKNOWLEDGMENTS

The authors express their appreciation to F. Palm and T. Pfannenmüller, EADS Deutschland GmbH, Ottobrunn, for providing the FSW material. The experimental assistance of Mr. M. Hühner and Mrs. I. Wittkamp is greatly appreciated. We also thank Professors E. Hornbogen and G. Eggeler, Ruhr-University Bochum, and Dr. A.K. Mukhopadhyay, Defense Metallurgical Research Laboratory, Hyderabad, for stimulating discussions.

REFERENCES

1. K.-H. Rendigs: *Mater. Sci. Forum*, 1997, vol. 242, pp. 11-24.
2. S. Kallee and A. Mistry: *Symp. on Friction Stir Welding*, Thousands Oaks, CA, 1999.
3. O.T. Midling, J.S. Kvåle, and O. Dahl: *Symp. on Friction Stir Welding*, Thousands Oaks, CA, 1999.
4. W.M. Thomas, E.D. Nicholas, J.C. Needham, M.G. Church, P. Templesmith, and C.J. Dawes: International Patent, Application No. PCT/GB92, Patent Application No. 9,125,978.8, 1991.
5. E.D. Nicholas and W.M. Thomas: *Int. J. Mater. Product Technol.*, 1998, vol. 13, pp. 45-54.
6. K.V. Jata, K.K. Sankaran, and J.J. Ruschau: *Metall. Mater. Trans. A*, 2000, vol. 31A, pp. 2181-92.
7. E. Schofer: *Mat.-wiss. Werkstofftech.*, 1999, vol. 30, pp. 693-96.
8. M.W. Mahoney, C.G. Rhodes, J.G. Flintoff, R.A. Spurling, and W.H. Bingel: *Metall. Mater. Trans. A*, 1998, vol. 29A, pp. 1955-64.
9. C. Dalle Donne, R. Braun, G. Staniek, A. Jung, and W.A. Kaysser: *Mat.-wiss. Werkstofftech.*, 1998, vol. 29, pp. 609-17.
10. Y. Li, L.E. Murr, and J.C. McClure: *Scripta Mater.*, 1999, vol. 40, pp. 1041-46.
11. Y. Li, L.E. Murr, and J.C. McClure: *Mater. Sci. Eng.*, 1999, vol. A271, pp. 213-23.
12. A.P. Reynolds, T.U. Seidel, and M. Simonsen: *Symp. on Friction Stir Welding*, Thousands Oaks, CA, 1999.
13. K.V. Jata: *Mater. Sci. Forum*, 2000, vols. 331–337, pp. 1701-12.
14. H. Jin, C. Ko, S. Saimoto, and P.L. Threadgill: *Mater. Sci. Forum*, 2000, vols. 331–337, pp. 1725-30.
15. A.P. Reynolds, W.D. Lockwood, and T.U. Seidel: *Mater. Sci. Forum*, 2000, vols. 331–337, pp. 1719-24.
16. A.F. Norman, I. Brough, and P.B. Prangnell: *Mater. Sci. Forum*, 2000, vols. 331–337, pp. 1713-18.
17. P. Dong, F. Lu, J.K. Hong, and Z. Cao: Paper presented at the *Int. Symp. Friction Stir Welding*, Thousands Oaks, CA, 1999.
18. Y.J. Chao and X. Qi: Paper presented at the *Int. Symp. on Friction Stir Welding*, Thousands Oaks, CA, June 1999.
19. I.J. Polmear: *Light Alloys—Metallurgy of the Light Metals*, 3rd ed., Arnold, London, 1995, pp. 112-14.
20. Y.S. Sato, H. Kokawa, M. Enomoto, and S. Jogan: *Metall. Mater. Trans. A*, 1999, vol. 30A, pp. 2429-2437.
21. G.A. Edwards, K. Stiller, G.L. Dunlop, and M.J. Couper: *Acta Mater.*, 1998, vol. 46, pp. 3893-3904.
22. K. Matsuda, H. Gamada, K. Fujii, Y. Uetani, T. Sato, A. Kamio, and S. Ikeno: *Metall. Mater. Trans. A*, 1998, vol. 29A, pp. 1161-67.
23. M. Murayama and K. Hono: *Acta Mater.*, 1999, vol. 47, pp. 1537-48.
24. S.J. Andersen, H.W. Zanderbergen, J. Jansen, C. Traeholt, U. Tundal, and O. Reiso: *Acta Mater.*, 1998, vol. 46, pp. 3283-98.
25. A. Perovic, D.D. Perovic, G.C. Weatherly, and D.J. Lloyd: *Scripta Mater.*, 1999, vol. 41, pp. 703-08.
26. C. Cayron and P.A. Buffat: *Acta Mater.*, 2000, vol. 48, pp. 2639-53.
27. D.J. Chakrabarti, B. Cheong, and D.E. Laughlin: *Automotive Alloys II*, Proc. TMS Annual Meeting, San Antonio, TX, Feb. 1998, S.K. Das, ed., TMS, Warrendale, PA, pp. 27-44.
28. C. Cayron and P.A. Buffat: *Mater. Sci. Forum*, 2000, vols. 331–337, pp. 1001-06.
29. G. Liu, C.-S. Niou, J.C. McClure, and F.R. Vega: *Scripta Mater.*, 1997, vol. 37, pp. 355-61.
30. O.V. Flores: *Scripta Mater.*, 1998, vol. 38, pp. 703-08.
31. C.G. Rhodes, M.W. Mahoney, and W.H. Bingel: *Scripta Mater.*, 1997, vol. 36, pp. 69-75.
32. F. Palm: EADS Deutschland GmbH, Ottobrunn, Germany, private communication, 2000.
33. A.W. Bowen: *Mater. Sci. Technol.*, 1990, vol. 6, pp. 1058-71.
34. J. Hirsch and K. Lücke: *Acta Metall.*, 1988, vol. 36, pp. 2863-82.
35. K. Lücke and O. Engler: *Proc. 3rd Int. Conf. on Aluminum Alloys*, Trondheim, Norway, 1992, pp. 439-52.
36. R.D. Doherty, D.A. Hughes, F.J. Humphreys, J.J. Jonas, D. Juul Jensen, M.E. Kassner, W.E. King, T.R. McNelley, H.J. McQueen, and A.D. Rollett: *Mater. Sci. Eng.*, 1997, vol. A238, pp. 219-74.
37. S. Gourdet, E.V. Konopleva, H.J. McQueen, and F. Montheillet: *Mater. Sci. Forum*, 1996, vols. 217–222, pp. 441-46.
38. H.J. McQueen, E. Evangelista, and M.E. Kassner: *Z. Metallkd.*, 1991, vol. 82, pp. 336-45.
39. F.J. Humphreys and M. Hatherly: *Recrystallization and Related Annealing Phenomena*, Elsevier Science Ltd., Oxford, United Kingdom, 1996, pp. 369-77.
40. L.F. Mondolfo: *Aluminum Alloys—Structure and Properties*, Butterworth and Co., London, 1976.